Q. J. R. Meteorol. Soc. (1999), **125**, pp. 225–252

The dynamics of heat lows

By ZSUZSANNA RÁCZ and ROGER K. SMITH*
University of Munich, Germany

(Received 12 January 1998; revised 10 June 1998)

SUMMARY

A numerical model is used to investigate dynamical aspects of the structure and evolution of a heat low in an idealized flow configuration with an area of land surrounded by sea. Of particular interest is the evolution of the distributions of relative vorticity and potential vorticity. While the heat low has a minimum surface pressure in the late afternoon following strong solar heating of the land, the relative vorticity is strongest in the early morning hours following a prolonged period of low-level convergence. Thus the heat low is not approximately in quasi-geostrophic balance. The low-level convergence is associated with the sea-breeze and later with the nocturnal low-level jet. The effects of differing sea area, land area and Coriolis parameter on various aspects of the heat low are investigated.

Although a cyclonic vortex, the heat low is characterized by an anticyclonic potential-vorticity anomaly relative to its environment throughout much of the lower troposphere on account of the greatly reduced static stability in the convectively well-mixed boundary layer; however, the surface temperature maximum over land corresponds with a cyclonic potential-vorticity anomaly at the surface. The reduced static stability in the mixed layer has the further consequence that the horizontal components of relative vorticity and horizontal potential-temperature gradient make a non-negligible contribution and of opposite sign to the potential vorticity in certain flow regions.

Two processes associated with the flow evolution in the model appear to be fundamental to understanding a range of low-level atmospheric phenomena over the arid interior of Australia: these are the deep convective mixing over land during the daytime and the development of a nocturnal low-level jet, which leads to convergence in the trough. Such phenomena include the diurnal behaviour of dry cold fronts and the generation of nocturnal wind surges and bores. It is reasonable to assume that similar processes operate in other arid regions of the world where deep convective mixing over land produces local maxima of diabatic heating in the lower atmosphere.

KEYWORDS: Heat low Heat trough Nocturnal jet Sea breeze Thermal low

1. INTRODUCTION

Heat lows or troughs are a prominent climatological feature of many arid land areas of the world during the warmer months, especially in low latitudes where insolation is at its peak. For example, they occur over northern and south-western Africa (Ramage 1971; Pedgley 1972; Griffiths and Soliman 1972), West Pakistan and northern India (Ramage 1971; Chang 1972; Joshi and Desai 1985), the Qinghai–Xizang plateau in China (Junning *et al.* 1986), south-western North America (Sellers and Hill 1974; Rowson and Colucci 1992; Douglas and Li 1996), Saudi Arabia (Ackerman and Cox 1982; Blake *et al.* 1983; Smith 1986a,b; Bitan and Sa'aroni 1992), Spain (Uriarte 1980; Gaertner *et al.* 1993; Alonso *et al.* 1994; Portela and Castro 1996) and north-western and north-eastern Australia (Moriarty 1955; Leslie 1980; Leighton and Deslandes 1991). Some authors refer to these systems as thermal lows or thermal troughs. Figure 1 shows mean-sea-level isobars and the corresponding isotherms at 850 mb for a typical situation over Australia. The heat low that forms in the easterlies over north-western Australia is a persistent climatological feature during the warmer months of the year. The effects of differential heating across the heat low are particularly evident in the 850 mb isotherm patterns.

Heat lows or troughs are shallow disturbances, generally confined below 700 mb. The distinction between a heat low and a heat trough has no dynamical significance and we will interchange the terms; the former has at least one closed isobar in the surface chart while the latter has the form of an open wave, a distinction that may depend on the isobar spacing in use. Both types of disturbance may be thought of as low-level cyclonic relative-vorticity maxima which are linked to horizontal gradients of diabatic heating.

* Corresponding author: Meteorological Institute, University of Munich, Theresienstr. 37, 80333 Munich, Germany.
e-mail: roger@meteo.physik.uni-muenchen.de

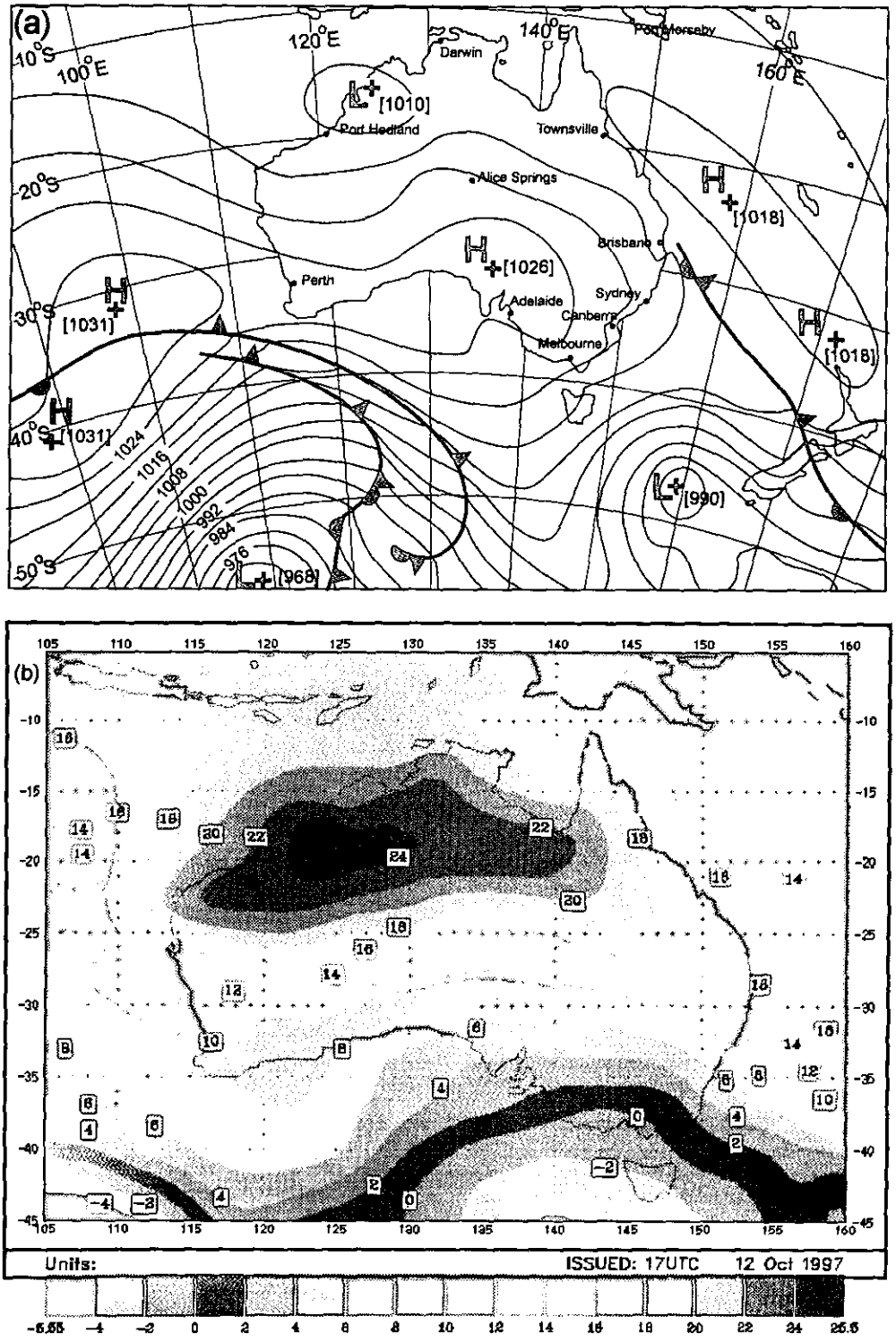

Figure 1. (a) Mean-sea-level pressure for the Australian region at 21 UTC 12 October 1997 showing a typical heat low over north-western Australia. (b) Isotherms at 850 mb at 11 UTC on the same day.

Blake *et al.* (1983, p. 1774) expressed the opinion that '. . . the numerical simulation of the detailed kinematic and thermodynamic structure of the heat low is an important unresolved problem'. Since that time, simple idealized models of the heat troughs that form over Australia have been described by Fandry and Leslie (1984) and Kepert and Smith (1992), while Gaertner *et al.* (1993) have studied the heat low that develops over the Iberian plateau using an idealized numerical model. An early attempt to model the summer heat low over Australia numerically is discussed by Leslie (1980), while experiments in real-time forecasting of the Western Australian summertime trough using a regional numerical model are described by Leslie and Skinner (1994). More recently, Alonso *et al.* (1994) and Portela and Castro (1996) describe three-dimensional numerical simulations of summer thermal lows over the Iberian peninsula. Analytical studies of the inland heat trough over Australia using linear wave theory are described by Adams (1986, 1993).

Based on their analyses of data for the heat low over Saudi Arabia, Blake *et al.* (1983) considered that the radiative sink of energy in the upper troposphere and the descending motion over much of the free troposphere would need to be incorporated in any satisfactory numerical model. To our knowledge these are not effects that have so far been included in idealized models and in view of the results presented here we would argue that it is more a detail than an order-one effect. Based on the mean-sea-level isobar fields, Portela and Castro (1996) suggest that the summertime heat low over the Iberian peninsula is strongest during the daytime and weakens or even disappears during the night. Their finding is supported by the present calculations, but as shown herein, one arrives at a different conclusion by examining the relative-vorticity field. Thus the heat low is not in quasi-geostrophic balance!

The present investigation was motivated by recent observational and numerical studies of the behaviour of dry cold fronts across central and northern Australia (e.g. Smith *et al.* 1995; Tory 1997). These fronts undergo a large diurnal variation of intensity. They are difficult to locate at the surface during the daytime when diabatic heating is at its peak, but experience strong frontogenesis during the evening and early morning leading to the formation of a sharp surface signature overnight. There is also evidence of an interaction between the heat trough over north-western Australia and the cold front as the latter moves across the continent, and this behaviour appears to explain the frequent development of a pre-frontal trough. Examination of relative-vorticity charts at 900 mb suggests that with the approach of the front, the heat trough becomes mobile and elongated as it moves south-eastwards ahead of the front to form the pre-frontal trough. Nocturnal frontogenesis then appears to take place in the pre-frontal trough so that this ends up becoming 'the front'.

The characterization of a heat trough as a cyclonic potential-vorticity (PV) maximum may provide a basis for understanding its interaction with a cold front (or with other weather systems) in terms of 'PV-thinking' (Hoskins *et al.* 1985), a possibility that leads us to enquire about the structure and evolution of PV in a heat trough. The Ertel PV is defined as

$$P = \frac{1}{\rho}\boldsymbol{\zeta}_a \cdot \nabla\theta, \tag{1}$$

where $\boldsymbol{\zeta}_a = \boldsymbol{\zeta} + f\mathbf{k}$ is the absolute vorticity, $\boldsymbol{\zeta}$ is the (three-dimensional) relative-vorticity vector, $f\mathbf{k}$ is the planetary vorticity vector, f is the Coriolis parameter, $\mathbf{k}$ is a unit vector in the vertical, ρ is the air density and θ is the potential temperature. In many situations, especially in the tropics, where horizontal temperature gradients are small, P is closely approximated by the contribution from the vertical component of absolute vorticity multiplied by the static stability-$(\partial\theta/\partial z)$ divided by ρ, but in the well-mixed boundary layer, $\partial\theta/\partial z$ is also small and the other terms in P may become comparatively more important. It

is therefore of interest to investigate the relative contributions of the horizontal and vertical vorticity terms to the PV. An analysis of the total PV-field and its evolution in a case-study of a thermal low over the Iberian peninsula is described by Alonso *et al.* (1994). They found the existence of a dome of negative PV up to 850 mb over the peninsula during the daytime due to the unstable thermal stratification, with low but positive PV values persisting during the night as the air re-stabilizes.

To investigate the basic dynamics of heat lows we describe a series of idealized numerical model experiments to study the structure and evolution of the heat low that forms in an otherwise still environment over a level heated land mass of regular shape surrounded by sea. Cases in which there is an environmental flow and/or orography will be considered in a subsequent paper. For the reasons noted above, questions concerning the structure and evolution of the PV distribution as well as other aspects of the heat low require the use of a model that has a sufficiently realistic representation of the dry convective boundary layer. The model we have selected is a version of that described by Leslie and Skinner (1994), but modified significantly by Tory (1997). Our calculations differ in one important respect from the numerical study of sea breezes over circular islands by Neumann and Mahrer (1974). Their largest horizontal domain size of 110 km (land and sea combined) is only slightly larger than our horizontal grid spacing (see section 2). In essence, we focus on the larger-scale aspects of the thermally driven sea-breeze circulation and do not seek to resolve the details of sea-breeze fronts.

The model is described briefly in section 2, and the experiments that are carried out are detailed in section 3. Results of the calculations are described in section 4 while section 5 contains the summary and conclusions.

2. The numerical model

The flow configuration in the model is shown in Fig. 2(a). The domain of interest is a rectangular column of air with a square horizontal cross-section extending through the depth of the atmosphere. A square region of land is located at the centre of the domain and is surrounded by sea. The flow is driven by diabatic processes associated with the diurnal cycle of heating and cooling of the land surface.

The model used is based on the hydrostatic primitive-equation numerical weather-forecast model described by Leslie *et al.* (1985) and developed further as detailed by Leslie and Skinner (1994). The present version has been modified for research purposes by Tory (1997). The model equations and method of solution are detailed in an appendix. Here we describe only the salient features necessary for interpreting the results.

The model is formulated in sigma coordinates (x, y, σ) on a southern hemisphere f-plane centred at 20°S latitude. Here $\sigma = p/p_s$, p is the pressure, and p_s the surface pressure. Although not necessary on an f-plane, we choose the x-axis pointing eastwards and the y-axis pointing northwards and refer to these as the zonal and meridional directions, respectively. The equations are expressed as finite-differences on a domain with 30 interior σ-levels which are unequally spaced to provide higher vertical resolution in the boundary layer as indicated in Fig. 2(b). The vertical grid is staggered, with the horizontal velocity components, geopotential and temperature stored at σ-levels and the vertical 'sigma' velocity, $\dot{\sigma} = \mathrm{D}\sigma/\mathrm{D}t$, stored half way between σ-levels. Here $\mathrm{D}/\mathrm{D}t$ is the material derivative defined in the appendix. A non-staggered Arakawa A-grid is used in the horizontal directions with all variables stored at each grid point. There are 41×27 grid points in the horizontal with a grid spacing of 100 km, giving a total domain size 4000 km west to east $\times$2600 km south to north. This is larger than the 2000×2000 km square domain of interest and is chosen to minimize the influence of the boundaries on the solution.

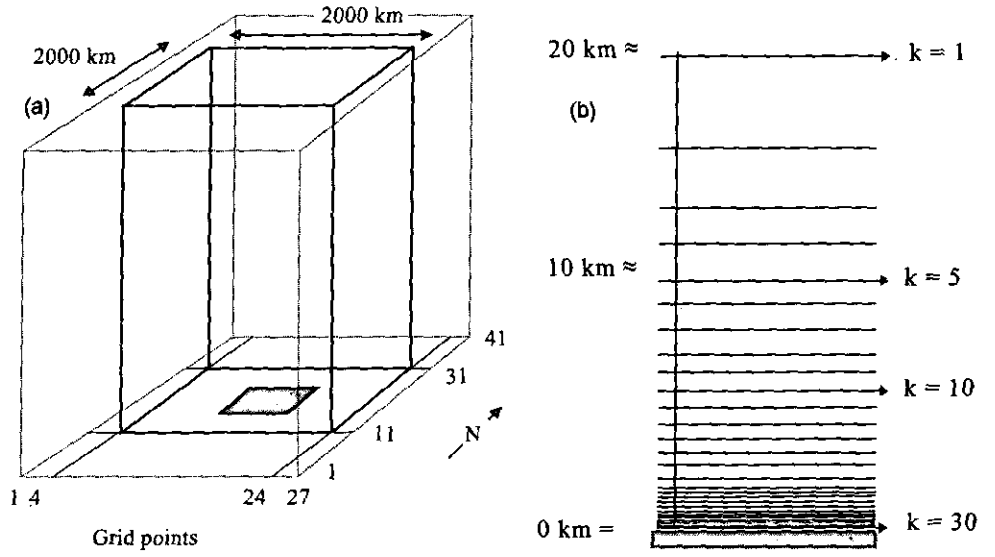

Figure 2. (a) The model domain for the main experiment (E1—see Table 1). The box marked by solid lines indicates the domain of interest. The outer box indicated by dotted lines is the computational domain. (b) Vertical levels in the model. The integer k is an index for the model σ-levels with $k = 1$ corresponding with the first level below the top of the domain at a height of approximately 20 km and $k = 30$ corresponding with the first level above the surface at a height of approximately 8 m.

(*a*) *Boundary conditions*

Periodic boundary conditions on the velocity components and temperature are assumed at the eastern and western boundaries, and channel boundary conditions at the northern and southern boundaries. The reasons for these conditions are more historical than necessary, and in the present calculations they are equivalent to impervious no-slip side boundaries all around the domain. We show in section 4(e) that by increasing the domain size while keeping all other parameters fixed the results to be described are not unduly influenced by these conditions; indeed the boundaries are in all cases not closer than about one-and-a-half Rossby deformation radii to the land, based on the static stability over the sea (see section 4(c)). At the upper boundary ($\sigma = 0$), $\partial u/\partial\sigma = 0$, $\partial v/\partial\sigma = 0$, $\partial T/\partial\sigma = 0$ and $\dot{\sigma} = 0$. At the lower boundary ($\sigma = 1$), $\dot{\sigma} = 0$ and the sea surface temperature is held constant. Other conditions are specified by the boundary-layer formulation described in the appendix and the formulation of diabatic processes considered next.

(*b*) *Diabatic processes*

The temperature of the ground over land during many diurnal cycles of heating and cooling is diagnosed from a surface heat balance condition. For maximum simplicity, there is no moisture in the model. Radiative processes are included only to the extent that they affect the surface energy budget; there is no direct absorption or emission of radiation from atmospheric layers, except for a simple representation of the atmospheric long-wave radiation to the surface. Thus, in the absence of cold-air advection, the formation of a surface-based stable layer over land at night can result only from mechanically forced turbulent heat loss to the ground. A heat diffusion equation is solved at three levels in the soil to compute the heat flux into or out of the ground. The surface parameters are detailed in Table A.1 in the appendix. The version of the scheme used has been verified by Tory

(1997) against data for days 33 and 34 of the Wangara boundary-layer experiment (Clarke *et al.* 1971).

3. Initial conditions and experimental design

The four numerical experiments described here are detailed in Table 1 and we refer to them in the text as E1, . . . , E4. Each experiment commences from a state of rest with the vertical potential-temperature profile shown in Fig. 3. This profile is based on the mean of data from 13 radiosonde soundings made in September 1991 at Townsville (146°E, 19°S), a coastal town on the north-eastern coast of Australia. Since the prevailing flow there is easterly, the profile is broadly typical of ocean conditions around northern Australia at the latitude of interest, although the idealized calculations are not meant to apply directly to Australia or any other specific location. Nevertheless, we note that the land area in E1 is comparable with that of the Iberian Peninsula. E2 is designed to investigate the sensitivity of the calculation E1 to the proximity of the lateral boundaries, while E3 is designed to delay or preclude sea-breeze penetration to the centre of the low. Finally E4 is designed to explore the effects of an increased rotational constraint, which may be expected to suppress

TABLE 1. The numerical experiments

	E1	E2	E3	E4
Land area (km^2)	600×600	600×600	1200×1200	1200×1200
Total area (km^2)	2000×2000	4000×4000	4000×4000	4000×4000
Coriolis	f	f	f	$2f$

Experiment E4 is identical to E3 except that the Coriolis parameter is doubled. Here $f = -4.988 \times 10^{-5}\ s^{-1}$

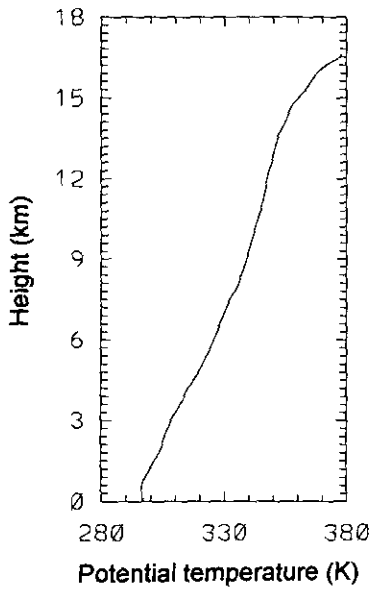

Figure 3. Vertical profile of potential temperature used as the initial condition for the model calculations.

TABLE 2. MAIN PHYSICAL PARAMETERS IN THE MODEL

Parameter	Value
Surface albedo	0.3
Sea surface temperature	25 °C
Latitude of the f-plane (except E4)	20°S

The surface albedo is typical of the arid region of north-western Australia.

further the inland penetration of the sea breeze, and to increase the rate of inertial turning it experiences. A few of the key parameters are listed in Table 2; a complete list is given in subsection (i) of the appendix—see Table A.1.

4. RESULTS

We begin with a description of the results from E1, starting with the flow evolution from the initial state and following with the mature stage.

(*a*) *Flow evolution*

After an initial period of adjustment lasting about 9 days, a repeatable diurnal cycle is established in the model integration. This cycle is illustrated by time series of selected quantities at the centre of the domain discussed in subsection (b). During the adjustment phase the diurnal mean pressure declines from its initial value of 1016 mb to reach a steady value of 1012.7 mb. During the same period, the maximum depth of the daytime mixed layer (the layer with approximately uniform potential temperature) progressively increases to reach a quasi-steady value. The relative vorticity shows also a marked diurnal variation in structure which becomes repeatable from day to day after a few days of integration. (Henceforth, except where the vector sense is clearly intended, we refer to the vertical component of relative vorticity simply as *the relative vorticity*.) Far from the land, at a corner of the inner domain, there is a very slight lowering of the isentropes with time in the lowest 600 m while at larger heights there is no perceptible change. Thus the initial sounding remains broadly representative of the far environment as the flow approaches a quasi-steady state. The slight warming at low levels occurs because the surface temperature of the initial sounding is a fraction of a degree cooler than the sea surface temperature.

Note that a true steady state cannot be attained without an external supply of cyclonic angular momentum from the environment because surface friction leads to a sink of cyclonic angular momentum for a heat low. The situation is similar to that of a tropical cyclone; in that case the source of angular momentum is presumed to be associated with an eddy transport from the environment associated with flow asymmetries (Anthes 1974, p. 511). In our model, and in most if not all axisymmetric tropical-cyclone models, the source of angular momentum is an artificial one associated with the lateral boundary conditions. The next subsection focuses on the structure of the quasi-periodic state that is attained in E1 after day 10.

(*b*) *The mature stage*

Figure 4 shows the surface pressure distribution near the time of maximum central surface pressure (0900 h—Fig. 4(a)) and the minimum surface pressure (1700 h—Fig. 4(b)). At the time of maximum central pressure, the isobar spacing is relatively uniform and

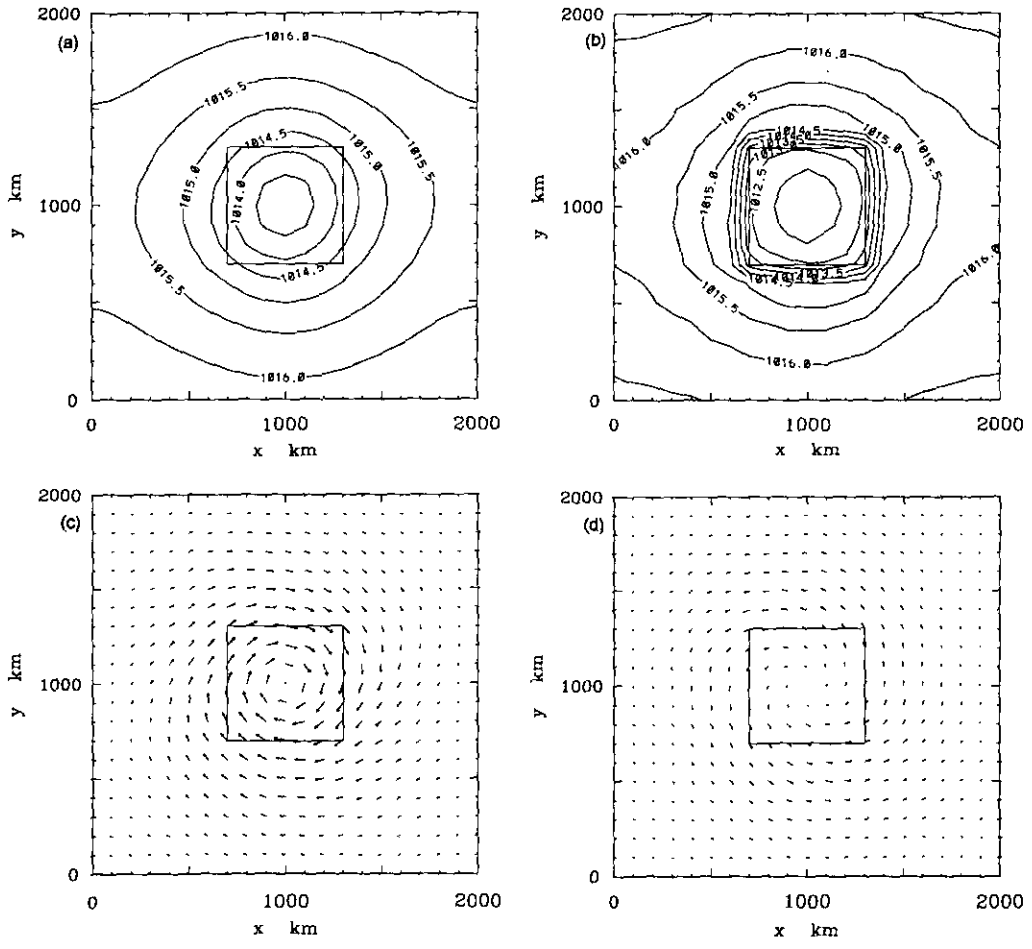

Figure 4. Isobars of surface pressure in experiment E1 at (a) 0900 h, and (b) 1700 h on the 11th day of model integration (characterizing the mature stage). These times are when the central surface pressure attains its diurnal maximum and minimum, respectively. Contour interval 0.5 mb. (c) Wind vectors at 0200 h on day 12 at a height of approximately 220 m. This time and height correspond with that for which the horizontal wind speed attains its maximum value. (d) Wind vectors at 0400 h on day 12 at a height of approximately 2.7 km. This time and height correspond with that for which the horizontal wind speed in the upper anticyclonic outflow is a maximum. The largest arrow in (c) corresponds with a wind speed of 10.2 m s^{-1}, and in (d) 5.0 m s^{-1}. The inner square indicates the region of land.

the isobars are approximately circular, despite the fact that the land mass is square. In contrast, at the time of minimum central pressure, the pressure gradient over the land is weak, but there is a strong gradient near the coast, a manifestation of the coastal sea breeze. Naturally, with the relatively coarse horizontal resolution used here, the sea-breeze front is not resolved. Figure 4(c) shows the wind vectors at the time of maximum horizontal wind (0200 h) and at the height at which the maximum occurs (220 m). The wind field at this time and height shows a symmetric azimuthal circulation about the domain centre, consistent with the broadly symmetric surface pressure field that develops during the night and early morning (Fig. 4(a)). This development is presumably associated with the natural tendency for vortices to axi-symmetrize (see, for example, Shapiro and Ooyama 1990; Smith *et al.* 1990). The wind vectors at the time (0400 h) of maximum meridional

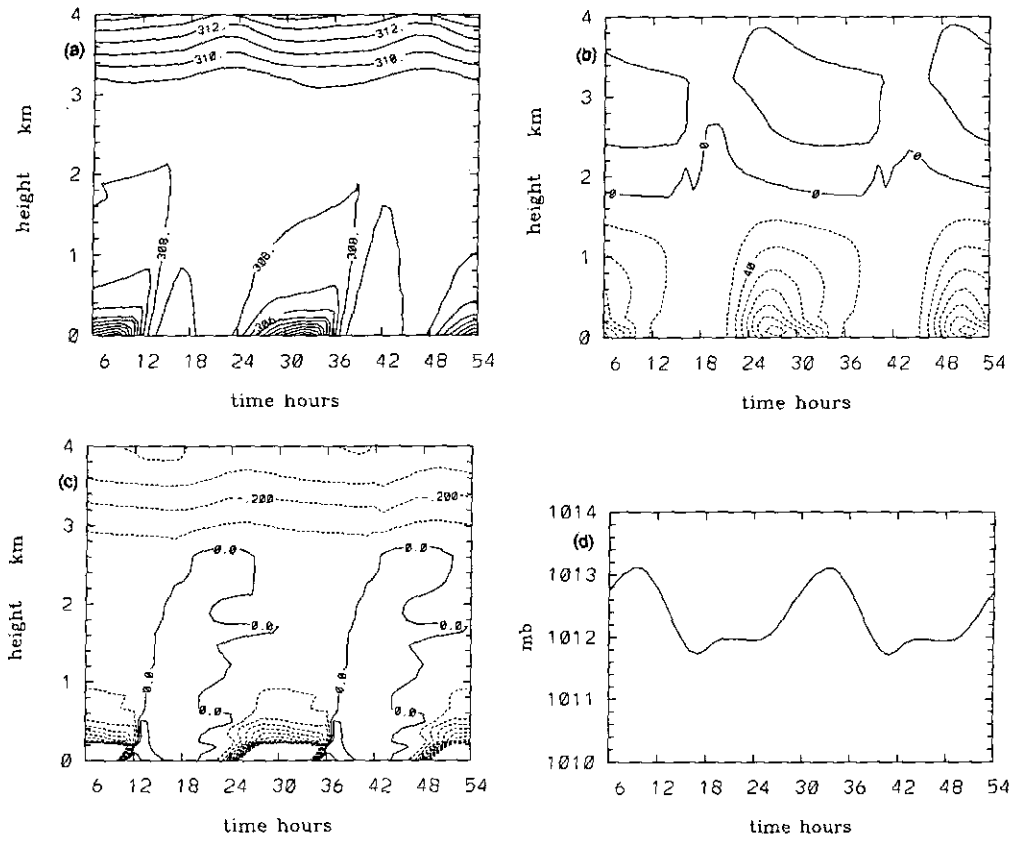

Figure 5. Time–height cross-sections in experiment E1 up to a height of 4 km of: (a) potential temperature, (b) relative vorticity, and (c) potential vorticity (PV) in the mature stage of the calculation, from 0600 h on day 11 to 0600 h on day 13. Contour intervals are 1 K in (a), 2×10^{-5} s^{-1} in (b), and 0.1 PV units in (c). Solid (dashed) contours indicate positive (negative) or anticyclonic (cyclonic) values. The near-surface region without contours in (c) indicates PV values less than −1.0 PV units. (d) Time series of surface pressure at the centre of the domain during this period.

motion aloft in the anticyclonic outflow layer and at the height at which this maximum occurs (2700 m) are shown in Fig. 4(d). Typically, the wind speeds are weaker than those in Fig. 4(c) and the radius at which the maximum occurs is larger.

Figure 5 shows height–time cross-sections of potential temperature, relative vorticity, and PV at the centre of the domain during a two-day segment in the mature stage of development (from 0600 h on day 11 to 0600 h on day 13). It shows also the time series of surface pressure at the centre of the domain during this period. All these fields show a regular and marked diurnal variation. The potential-temperature field is characterized by the development of a deep well-mixed layer during the afternoon, which reaches a depth of about 3 km, and the development of a low-level inversion during the night, which gradually deepens to about 200 m in the hour before sunrise. Erosion of the inversion commences near the surface at about 0900 h, some three hours after sunrise, but is not complete until around midday. During the afternoon, the air at the base of the mixed layer has an unstable lapse rate as is observed (see, for example, Stull 1988, p. 217). Stabilization of the near-surface layers recommences in the evening because of the mechanically forced turbulent heat

TABLE 3. A SUMMARY OF VARIOUS QUANTITIES CHARACTERIZING THE MATURE STAGE OF THE FOUR CALCULATIONS

	Experiment			
	E1	E2	E3	E4
ΔT(K)	35	35	37	38
p_{s-max} (mb)	1013.1	1012.5	1009.6	1008.9
$t_{(p_{s-max})}$ (h)	0900	1000	1100	0900
p_{s-min} (mb)	1011.7	1010.9	1008.8	1007.9
$t_{(p_{s-min})}$ (h)	1700	1700	1700	1600
Δp (mb)	1.4	1.6	0.8	1.0
v_{max} (m s^{-1})	9.3	9.6	13.3	10.9
$t_{(v_{max})}$ (h)	0200	0200	0400	0000
ζ_{min}(s^{-1})	-15.8×10^{-5}	-15.9×10^{-5}	-11.8×10^{-5}	-5.3×10^{-5}
$t_{(\zeta_{min})}$ (h)	0400	0400	0700	0200

ΔT is the difference between the maximum and minimum temperature at ground level at the centre of the domain during the diurnal cycle; p_{s-max} and p_{s-min} are the maximum and minimum surface pressure at the centre of the domain, and $t_{(p_{s-max})}$ and $t_{(p_{s-min})}$ are the times when these occur; $\Delta p = p_{s-max} - p_{s-min}$; v_{max} is the maximum meridional velocity, ζ_{min} is the minimum relative vorticity (i.e. maximum cyclonic) and $t_{(v_{max})}$ and $t_{(\zeta_{min})}$ are the times at which these occur. In all cases the maximum meridional velocity occurs at a height of 220 m and the maximum relative vorticity at a height of 100 m.

flux to the cooler ground surface. As a result the nocturnal inversion gradually deepens, reaching its maximum depth around sunrise. The inversion and mixed-layer depths are characteristic of those observed over central Australia, for example, during the late dry season (see, for example, Smith *et al.* 1995).

The relative vorticity is comparatively weak during the period of strong mixing, but its magnitude increases steadily after sunset, reaching a maximum at 0400 h at a height of about 100 m, suggestive of a connection with the nocturnal low-level jet (see later). The vorticity is cyclonic below 2 km and anticyclonic above this level. The maximum anticyclonic vorticity occurs at a height of 2.7 km and somewhat later at 0600 h.

The PV at the centre of the domain is small throughout most of the depth of the mixed layer during the daytime on account of the extremely small static stability, but it develops a strong signature near the surface during the night-time on account of the stabilization associated with the radiative cooling of the land (Fig. 5(c)). Above the mixed layer the PV increases in magnitude with height.

The surface pressure at the centre of the domain (Fig. 5(d)) has a diurnal maximum at about 0900 h and a minimum at 1700 h, the amplitude of the diurnal variation being about 1.4 mb. Table 3 provides a summary of various quantities characterizing the mature stage of the four calculations and will be referred to repeatedly later.

Vertical west–east cross-sections of potential temperature and the zonal-, meridional-, and vertical-velocity components at 1500 h on day 11 are shown in Fig. 6 up to a height of 4 km. Similar cross-sections at 2100 h, and at 0300 h and 0900 h on day 12, are shown in Figs. 7, 8 and 9, respectively. Afternoon conditions, exemplified by the fields at 1500 h, show a convectively well-mixed layer over the land about 3.0 km deep, with a slightly unstable stratification in the lower half and a slightly stable one in the upper half. Over the sea the stratification is stable with the strongest stability at low levels. The zonal velocity pattern shows regions of strong onshore flow near the two coastlines with a maximum speed of 4.8 m s^{-1}, essentially marking the coastal sea breezes. Aloft there is an offshore

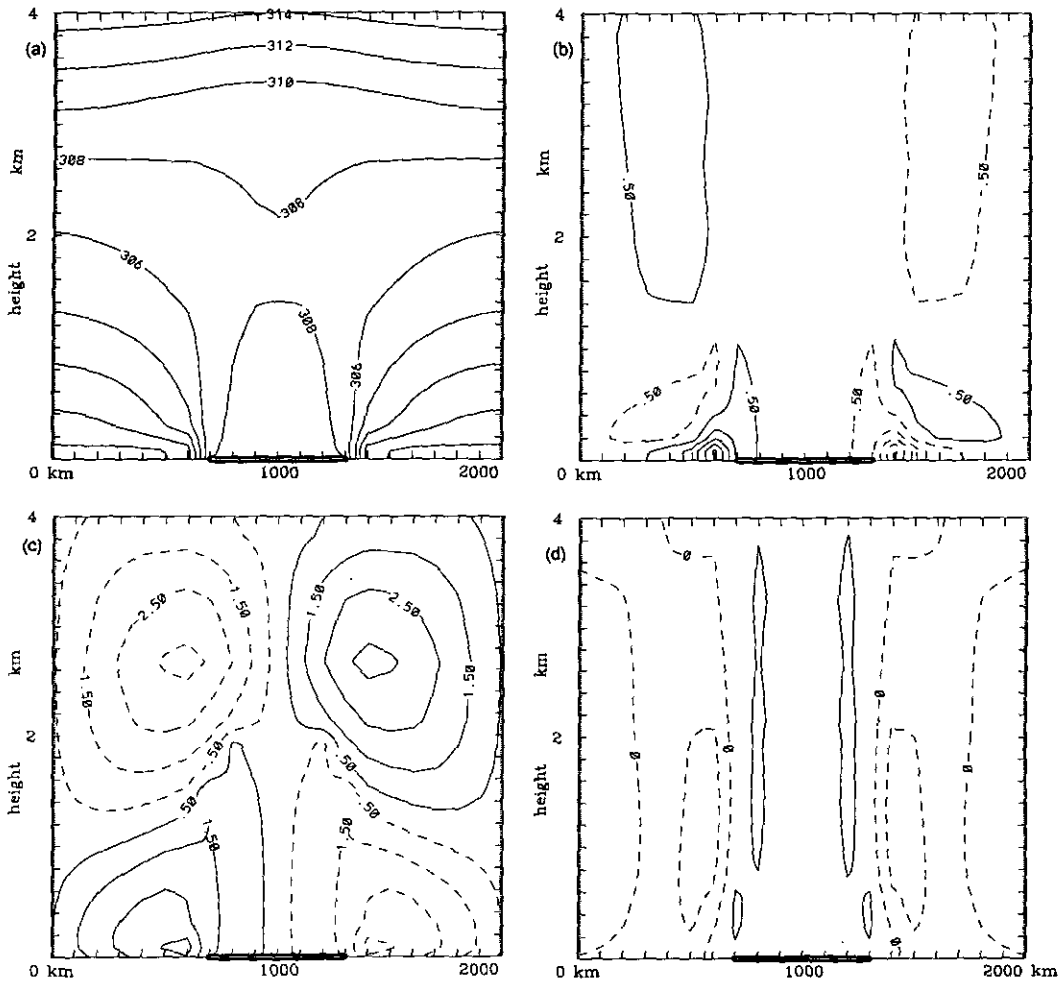

Figure 6. Vertical west–east cross-section through the centre of the domain in experiment E1 up to a height of 4 km of: (a) potential temperature, and (b), (c) and (d), the zonal-, meridional-, and vertical-velocity components, respectively, at 1500 h on day 11. Contour interval is 2 K in (a), 1 m s^{-1} in (b) and (c), and 0.5 cm s^{-1} in (d). Solid (dashed) contours indicate positive (negative) velocity components and ascending (descending) vertical velocities. The thick solid line on the base of each panel shows the land surface.

return flow extending to a height of about 1.5 km. Above this level to at least 4 km there is a region of weak onshore flow, principally over the sea. This is a remnant of the late-morning flow in the quasi-periodic state as exemplified in Fig. 9 (see especially Figs. 9(b) and (d)). The meridional flow at this time shows a relatively weak cyclonic circulation up to 2 km with the maximum of 3.9 m s^{-1} occurring near the coast at a height of 150 m. Over the land the gradient of both horizontal-velocity components is relatively small on account of the strong vertical mixing of momentum by the convectively generated turbulence in the mixed layer. The main signature in the vertical-velocity field at this time is the region of subsidence just offshore, which is largely a remnant of the late-morning flow, but may be strengthened at low levels by the subsiding branch of the sea breeze.

The mixed layer over land continues to deepen during the late afternoon (Fig. 6(a)) and at 2100 h it is around 3.2 km in height (Fig. 7(a)). By this time the slightly unstable region

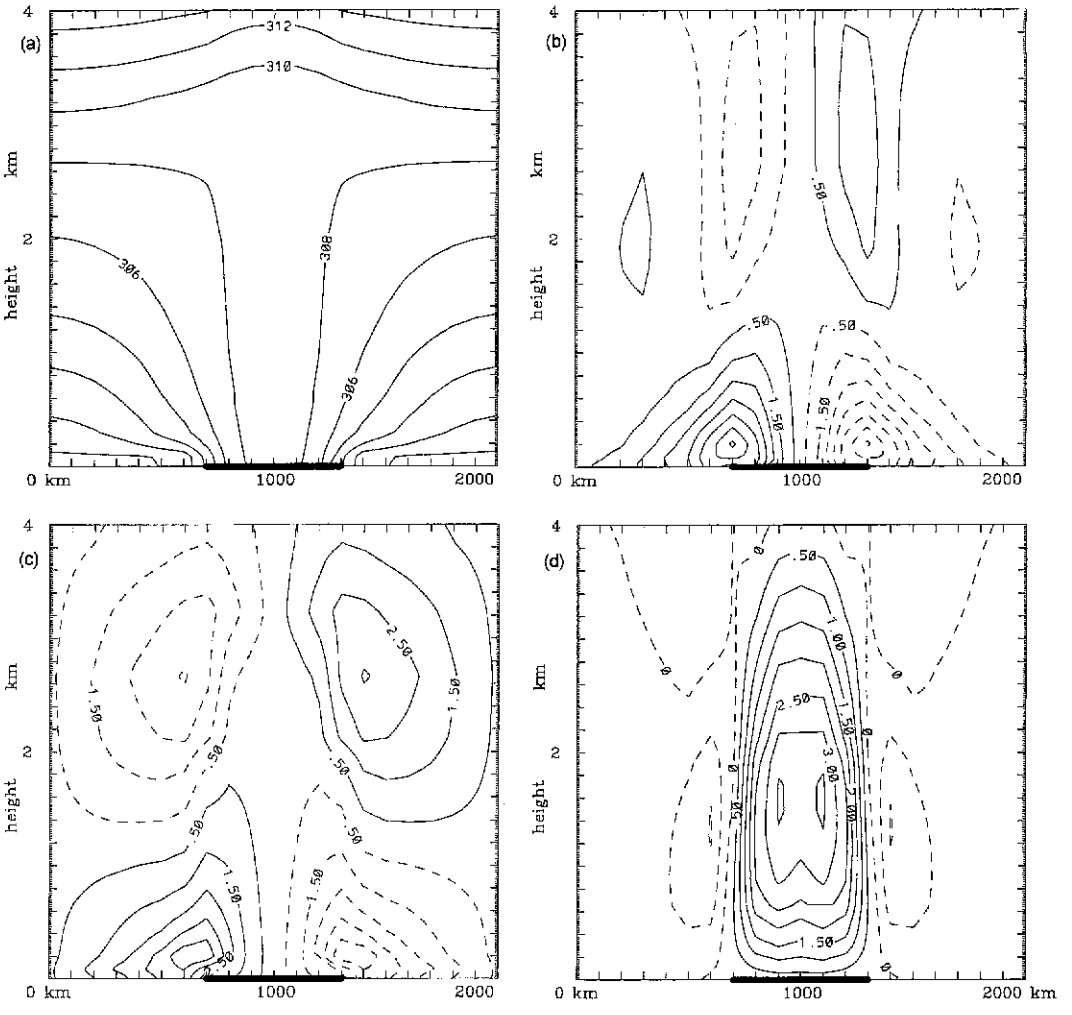

Figure 7. As Fig. 6, except for 2100 h on day 11.

has disappeared and the near-surface layer has begun to stabilize. The onshore flow which was previously associated with the sea breeze has further strengthened and indicates the transformation into a nocturnal low-level jet (Fig. 7(b)), a component of which is evident in the meridional-velocity field also (Fig. 7(c)). The maximum zonal wind speed in the jet is 6.7 m s^{-1}, an increase of 1.9 m s^{-1} from the sea breeze at 1500 h, and it is located a little inland at a height of 200 m. There is now marked outflow in the upper part of the mixed layer over land, although there is still some remnant of the region of weak onshore flow aloft over the sea. The meridional velocity has strengthened also, the maximum being now 5.4 m s^{-1} at a height of 250 m. By evening there has been a dramatic increase in the vertical velocity of air within the mixed layer over land, the maximum occurring at about 1.8 km, a little more than half the depth of the mixed layer. The subsidence over the sea has marginally strengthened also, but is largely confined to the near-coastal region, suggesting that the 'wall' boundary conditions have a minimum influence on the realism of the solution in the inner part of the domain (see also subsection 4(e)).

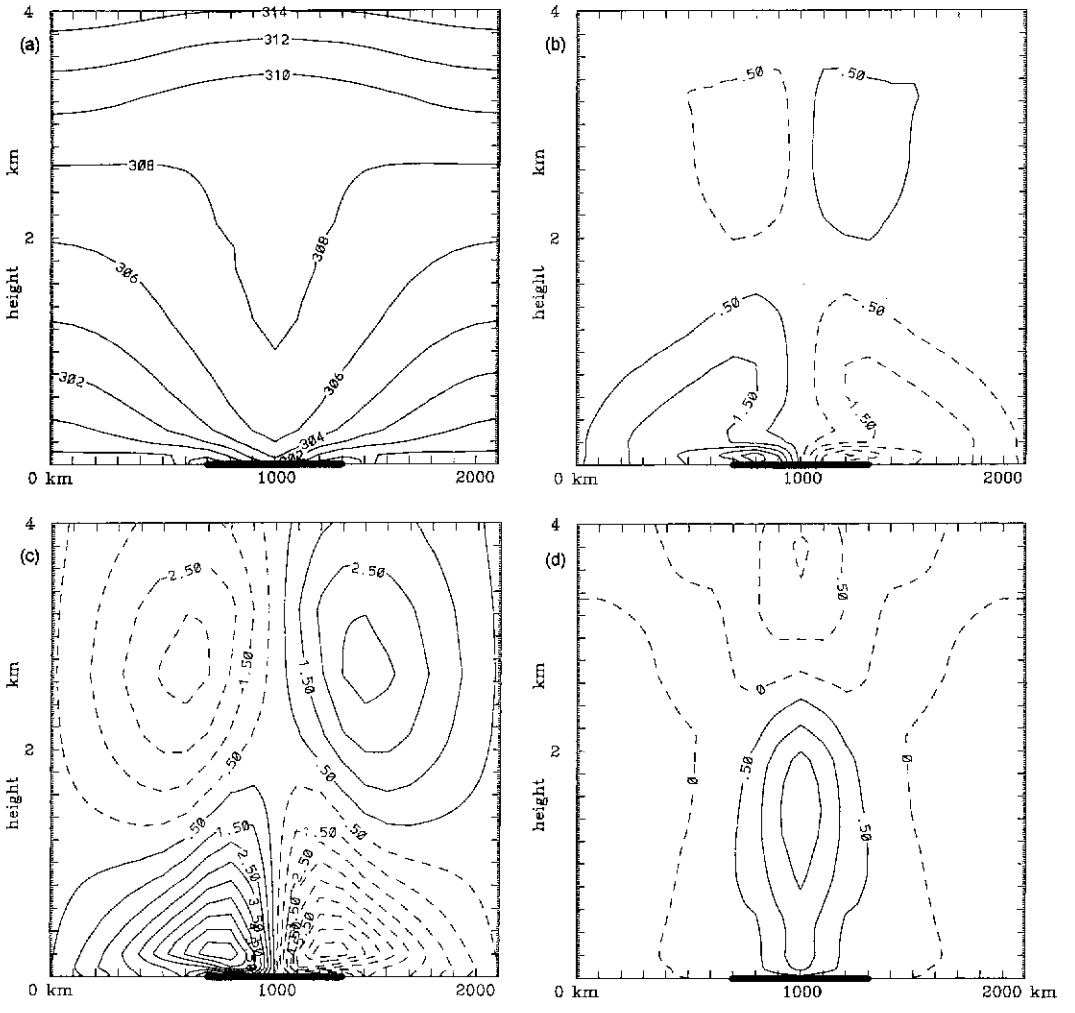

Figure 8. As Fig. 6, except for 0300 h on day 12.

The most striking development takes place during the following 6 hours as indicated by the fields at 0300 h on day 12 shown in Fig. 8. The air over the land has stabilized at low levels on account of the continued inland penetration of sea-breeze air and the continued turbulent transport of heat to the radiatively cooled ground. The stabilization is accompanied by the formation of a pronounced nocturnal low-level jet over the land which is evident in both the zonal and meridional velocity components. The maximum zonal velocity at this time has decreased to about 5 m s^{-1}, but has moved to within 100 km of the domain centre at a height of barely 100 m. In contrast, the maximum meridional velocity has increased to 9.3 m s^{-1} and occurs at a height of 220 m. The maximum vertical velocity has decreased since 2100 h and there is now a region of subsidence above 3 km over the land.

At 0900 h the isentropes show a near-surface stable layer over the land underlying a weakly-stable layer, over 3 km deep, a remnant of the previous day's well-mixed layer. The

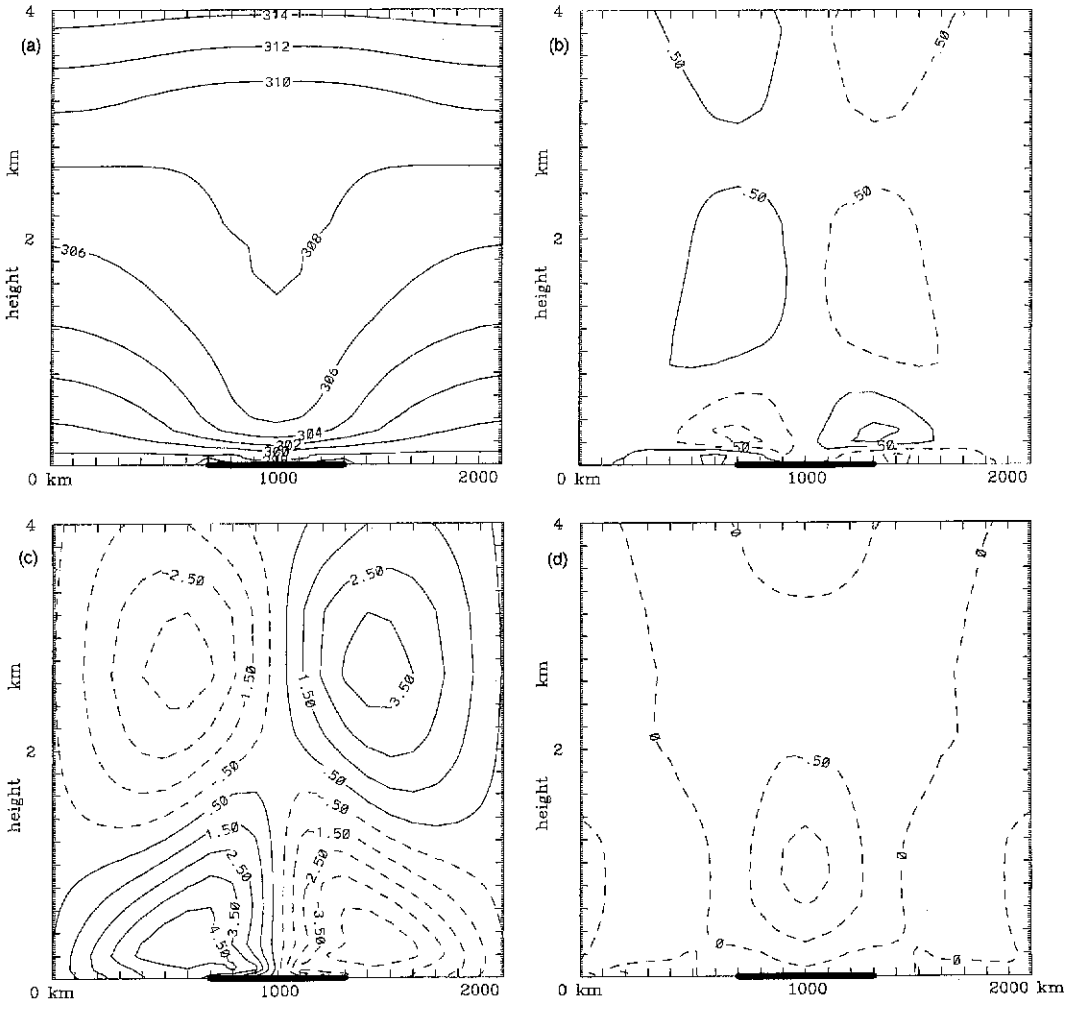

Figure 9. As Fig. 6, except for 0900 h on day 12.

zonal velocity still shows inflow in the lowest 150 m, with outflow up to about 800 m. The inflow is associated with the remnants of the nocturnal low-level jet and the outflow above marks the return seawards circulation. Above 800 m there is weak inflow (Fig. 9(b)) with subsidence over the land (Fig. 9(d)) feeding also into the outward branch of the circulation above the remnants of the low-level jet. The meridional velocity is cyclonic up to about 1.6 km over the land, but the maximum of just over 5.4 m s^{-1} occurs at a height of 300 m.

(c) *Relative vorticity and potential vorticity*

West–east height cross-sections of relative vorticity and PV at 1500 h and 0300 h are shown in Fig. 10. At 1500 h over the land the relative vorticity is cyclonic up to 2 km, with isolated maxima near the coast and near the centre of the domain, and anticyclonic above this level. (Note that solid contours denote cyclonic vorticity which is negative by convention in the southern hemisphere.) The PV is effectively zero in the lower half of the

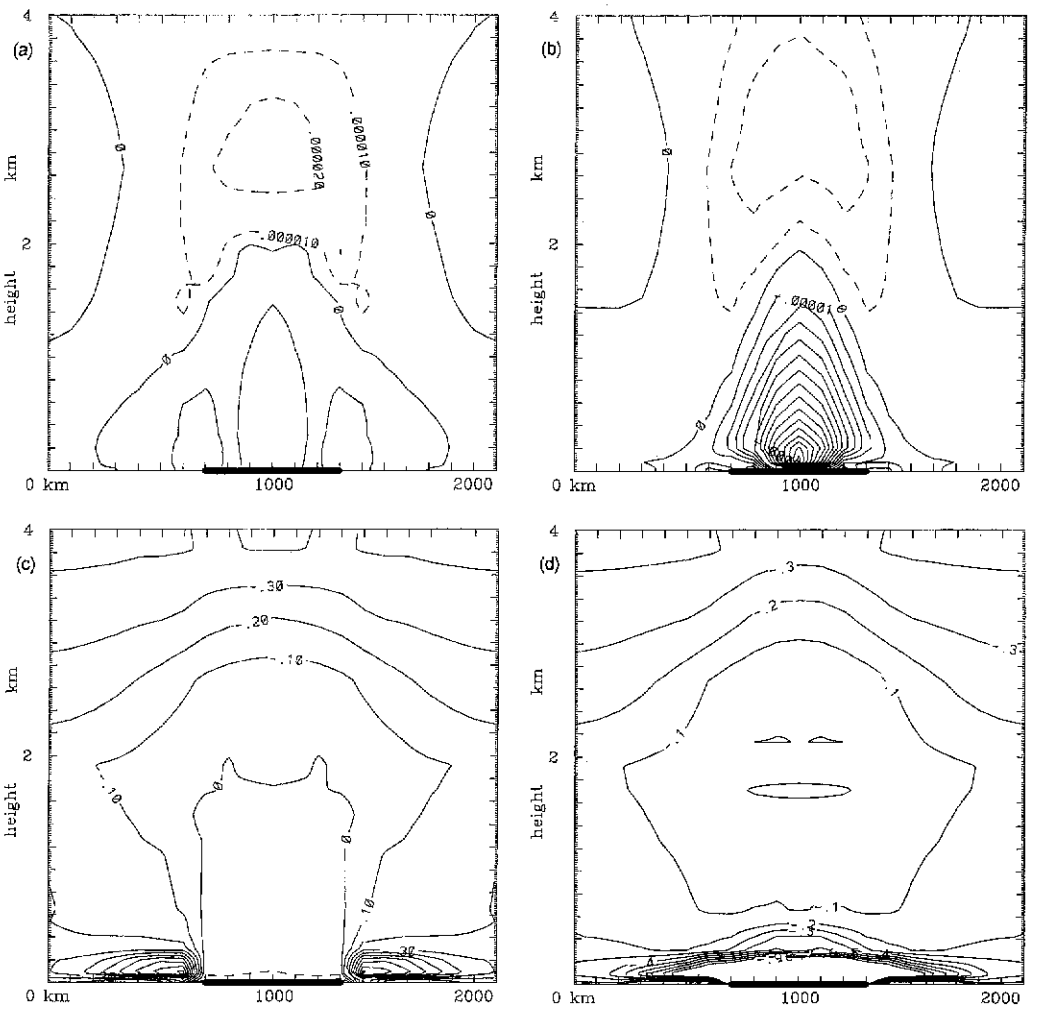

Figure 10. West–east vertical cross-section through the centre of the domain in experiment E1 up to a height of 4 km of relative vorticity at (a) 1500 h on day 11 and (b) 0300 h on day 12, and potential vorticity (PV) at (c) 1500 h on day 11 and (d) 0300 h on day 12. Solid (dashed) contours indicate cyclonic (anticyclonic) values which are negative (positive) in the southern hemisphere. Contour interval is 1×10^{-5} s^{-1} for relative vorticity and 0.1 PV units for potential vorticity. The near-surface region without contours in (c) and (d) indicates PV values less than −1.0 PV units, The thick solid line on the base of each panel shows the land surface.

mixed layer over the land, mostly on account of the neutral stratification (see subsection (d)) and is slightly positive near the surface where the stratification is unstable. It is strongly negative (i.e. cyclonic) in a shallow layer over the sea, mostly on account of the enhanced static stability of the air in the onshore sea-breeze flow. At levels above 2 km the pattern is more a reflection of the initial PV distribution, but is distorted principally over land because of the relative vorticity and the modified static stability, which is slightly positive in the upper half of the mixed layer.

As indicated in Table 3, the minimum* relative vorticity occurs at 0400 h, some 2 hours later than the maximum meridional wind speed, which for this experiment is 9.3 m s^{-1}.

* Maximum in amplitude.

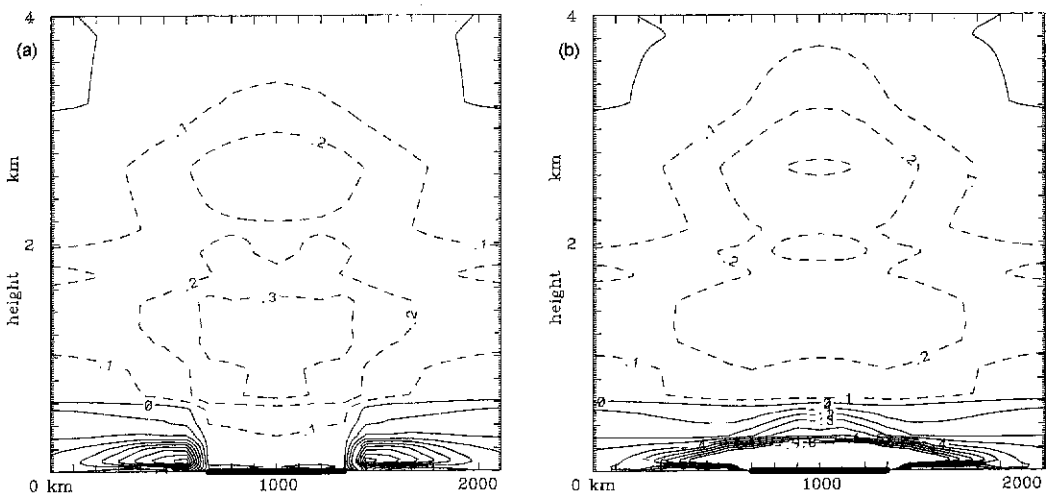

Figure 11. As Fig. 10 except for perturbation potential vorticity; (a) at 1500 h and (b) at 0300 h. Solid (dashed) contours indicate cyclonic (anticyclonic) perturbations. Contour interval is 0.1 PV units.

The strengthening of the low-level inflow during the late afternoon and evening is accompanied by an increase in the relative vorticity at low levels, and by 2100 h the two low-level maxima associated with the sea breeze have moved 100 km inland (figures not shown). There is little change in the strength of the anticyclonic vorticity, but the region of anticyclonic vorticity deepens, presumably because of the deepening of the mixed layer, itself. In contrast to these changes, the changes in the PV distribution are relatively small, although the PV increases in a shallow surface layer, mainly over the sea, mostly on account of the increasing vertical gradient of the horizontal wind (figure not shown).

A dramatic increase in the relative vorticity takes place in the late evening and early morning as evidenced by the field at 0300 h (Fig. 10(b)). At this time there is a single low-level maximum at about 100 m above the surface. The change is less pronounced in the PV distribution because the static stability aloft is still comparatively small over the land. However, the stabilization of air at low levels near the centre of the domain does have a noticeable effect on the PV field. The relative-vorticity pattern at 0900 h (figure not shown) is similar to that at 0300 h, but the amplitude is appreciably weaker. Again the most major change to the PV field during this time is associated with a further increase in static stability in the lowest 200 m near the centre of the domain and an increase in the vertical gradient of the horizontal wind in this region. Similar patterns of PV were found by Alonso *et al.* (1994) in a case-study of the Iberian thermal low. They refer specifically to a zone of negative PV at 1000 mb and 850 mb associated with the diabatic heating over land and a positive anomaly which '. . . is mainly related to the strong static stability over the sea'. The occurrence of negative* PV as high as 850 mb in their case may be partly a result of the elevated terrain over the Iberian peninsula as the depth of the well-mixed layer over the peninsula is only about 2 km.

Figure 11 shows the perturbation PV field at 1500 h and 0300 h, that is the current PV distribution minus that in the initial state. Note that the major feature is a positive (i.e. anticyclonic) PV anomaly associated with the heat trough over land, and a negative anomaly at low levels associated at 1500 h with the enhanced static stability over the sea,

* In their northern hemisphere case, negative PV means anticyclonic.

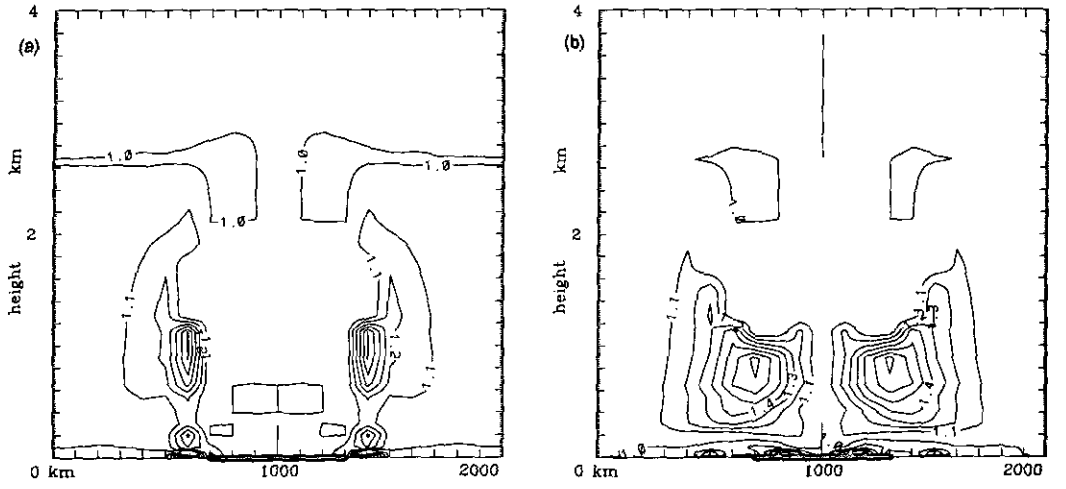

Figure 12. As Fig. 10 except for the absolute value of the ratio of the contribution to the total potential vorticity from the vertical components of the relative-vorticity vector and horizontal potential-temperature gradient: (a) at 1500 h and (b) at 0300 h. Contour interval is 0.1.

and at 0300 h with the enhanced low-level stability also over the land. The existence of an anticyclonic PV anomaly in the presence of a cyclonic circulation may seem contradictory at first sight, but one should bear in mind that the localized maximum of surface temperature at the domain centre is associated with a cyclonic PV anomaly.

(*d*) *Relative contributions to the potential vorticity*

One question that arose in the present study concerns the relative contribution of the horizontal and vertical components of the relative-vorticity vector and the potential-temperature gradient to the PV in Eq. (1), especially over land where the static stability is small or even slightly negative in the convectively well-mixed layer. Figure 12 shows contours of the absolute value of the ratio of the contribution to the PV from the vertical components of the relative-vorticity vector and potential-temperature gradient to the PV itself at 1500 h on day 11 and 0300 h on day 12. Below 2 km the ratio shows significant deviations from unity depending on the time of day. At 1500 h the deviations are confined mainly to a region over the sea, just offshore, while at 0300 h they are more widespread. The largest deviations actually occur at 2100 h when the maximum value of the ratio exceeds 2.5. It follows that the contribution to the PV from the horizontal components of the relative-vorticity vector and potential-temperature gradient is not everywhere negligible in the lowest 2 km, where vertical shear and horizontal temperature gradient can be appreciable; moreover the contribution is of opposite sign to that from the vertical terms in the expression for PV.

(*e*) *The effects of domain size*

Experiment E2 was carried out to investigate the influence of the domain boundaries on the results of E1. The only difference in this calculation is that the linear dimension of the domain of interest is twice that of E1, the land size being the same. It turns out that the differences between the two calculations are relatively small, as indicated, for example, by a comparison of columns 2 and 3 of Table 3. This similarity is also evident

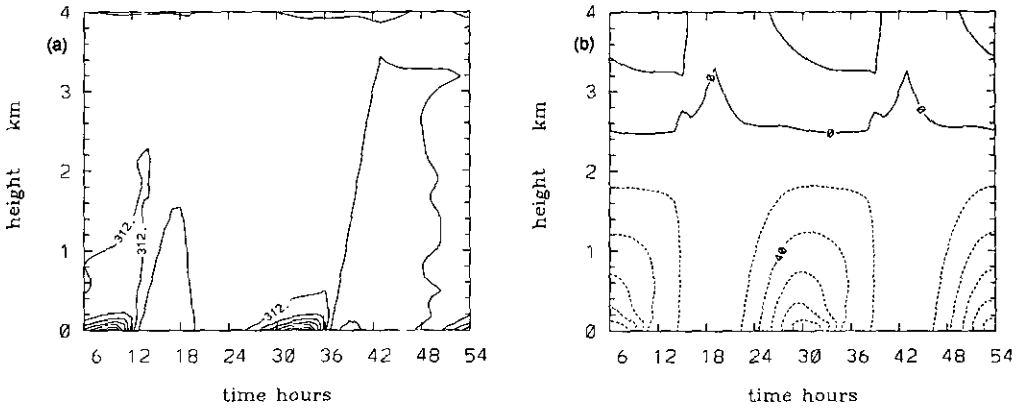

Figure 13. Time–height cross-sections up to a height of 4 km of (a) potential temperature, and (b) relative vorticity in the mature stage of the calculation E3, from 0600 h on day 11 to 0600 h on day 13. Contour intervals are 1 K in (a) and 2×10^{-5} s^{-1} in (b) with negative values shown dashed.

when one compares the vertical west–east cross-sections of potential temperature and the three velocity components (figure not shown) with the corresponding ones for E1 shown in Figs. 6–10. The most noticeable differences are in the meridional (i.e. tangential) velocity field at large distances from the land. In each calculation the pattern of v-contours fills the domain, indicative that there is a torque at the side boundaries on account of the boundary condition that the velocity component parallel to the boundary is zero, as discussed in section 4(a). Also, the maximum and minimum values of this component are slightly larger in E2 than in E1. We conclude that the boundary influence is relatively small, notwithstanding the remarks made at the end of section 4(a) concerning the angular-momentum budget. This small influence is not too surprising when one calculates a characteristic deformation radius L_R over the sea for the half-layer* depth primarily affected by the heat-low circulation (say $H = 2$ km). Taking the Brunt–Väisälä frequency based on the initial† sounding in this layer ($N = 0.13$ s^{-1}), and the Coriolis parameter $f = 5 \times 10^{-5}$ s^{-1}, we find that $L_R = 520$ km. This is about two thirds the distance of the land from the nearest boundary in E1 and on the order of one third of this distance in E2–E4.

(*f*) *Larger land areas*

Experiment E3 was designed to investigate the effects of increasing the land area. It is identical to E2 except that the linear dimension of the land is twice as large. In this case the flow requires slightly longer to attain a quasi-steady state and the mature stage is typified by the flow behaviour on days 11 to 12. Figure 13 shows time–height cross-sections of potential temperature and relative vorticity at the centre of the domain on these days, which should be compared with Figs. 5(a) and (b). The nocturnal inversion at the centre of the domain is much weaker than in E1, presumably because cooler sea-breeze air takes longer to reach the centre. As a result, the inversion is destroyed much earlier in the day and the mixed-layer depth at the centre is larger than in E1. The magnitude of the relative-vorticity perturbation is only about three quarters of that in E1 and E2 (Table 3) and takes longer to be attained (0700 h compared with 0400 h in E1 and E2). Nevertheless, the vorticity is

* Note that the in-up-out circulation within the heat low corresponds roughly with a first internal mode in the layer affected, which suggests that the half depth is appropriate for estimating L_R.

† Recall that this sounding is close to that in the far-field (see subsection (a)).

spread over a larger area (not shown) and the maximum meridional velocity is about 30% larger than in E1 and E2, but is again reached later (0400 h compared with 0200 h in E1 and E2).

The vertical west–east cross-sections of potential temperature and the zonal-meridional-, and vertical-velocity components have patterns which are very similar to those in the corresponding cross-sections for E1 shown in Figs. 6–9 and for reasons of space are not shown. In brief, while the primary features of the zonal- and vertical-velocity components are confined to the land and adjacent sea areas, the meridional component extends over the entire domain, again indicative that there is a torque on the flow at the side boundaries. The maximum meridional velocity is larger than that in E1, but takes longer to be attained (Table 3). The cross-sections of relative vorticity at 1500 h and 0300 h (not shown) have patterns that are very similar to the corresponding ones in E1 shown in Figs. 10(a) and (b), but the maximum and minimum values are smaller than in E1 (see also Table 3).

The surface pressure patterns for this case at the times when the surface pressure at the domain centre is a maximum (in this case at 1100 h) and a minimum (as before at 1700 h) are similar to the corresponding patterns for E1 shown in Fig. 4 and therefore are not shown.

The diurnal evolution of the near-surface wind field (100 m high) is indicated in Fig. 14, which shows the wind vectors at 1500 h and 2100 h on day 11 and at 0300 h and 0900 h on day 12. At 1500 h the wind vectors indicate a strong flow near the coast, with a significant along-shore component in a cyclonic sense, and very light winds over the land. By 2100 h the wind direction has veered and the region of stronger winds has penetrated farther inland. Over the following six hours the vortical flow increases in strength and its scale contracts (Fig. 14(c)), after which time it progressively decays, the maximum speed decreasing by a third by 0900 h (Fig. 14(d)).

(*g*) *Larger Coriolis parameter*

Experiment E4 is identical to E3 except that the Coriolis parameter is doubled. This increase may be expected to inhibit the inland penetration of the sea breezes and to increase the along-shore wind component at low levels. That this is the case is illustrated in Fig. 15, which shows the low-level wind vectors at 2100 h on day 11, at 0300 h and 0900 h on day 12, and the corresponding surface pressure pattern at 0900 h on day 12, during the mature stage. The low-level wind vectors at 1500 h on day 11 are very similar to those for E3 shown in Fig. 14(a) and therefore are not shown. Comparison of the wind fields with the corresponding ones in Fig. 14 shows a less concentrated vortex over land with a pronounced azimuthal-wave-number-4 asymmetry persisting throughout the night. The larger inertial effects reduce the cyclonic inflow towards the centre of the domain and lead to trough-like features in the north-east, south-east, south-west and north-west directions where the lateral sea-breeze component leads to an offshore component of the flow. These changes are reflected also in the surface pressure field where the square-like pattern of early afternoon, exemplified by Fig. 4(b), remains throughout the night. This pattern is illustrated by the surface isobars at 0900 h on day 12 shown in Fig. 15(d). The increased inertial effects lead to a weaker vortex than in E3 as is seen by comparing the entries in columns 4 and 5 of Table 3. A similar type of behaviour is found in thermally driven vortex flows (Smith and Leslie 1975).

We do not find a fundamental difference in behaviour between experiments E3 and E4 on account of the fact that the inertial period is longer than one day in E3 (latitude 20°S) and shorter than one day in E4 (latitude 43°S). Such a difference was found in an analytic study of the linear, frictionless, sea-breeze problem by Rotunno (1983). In the

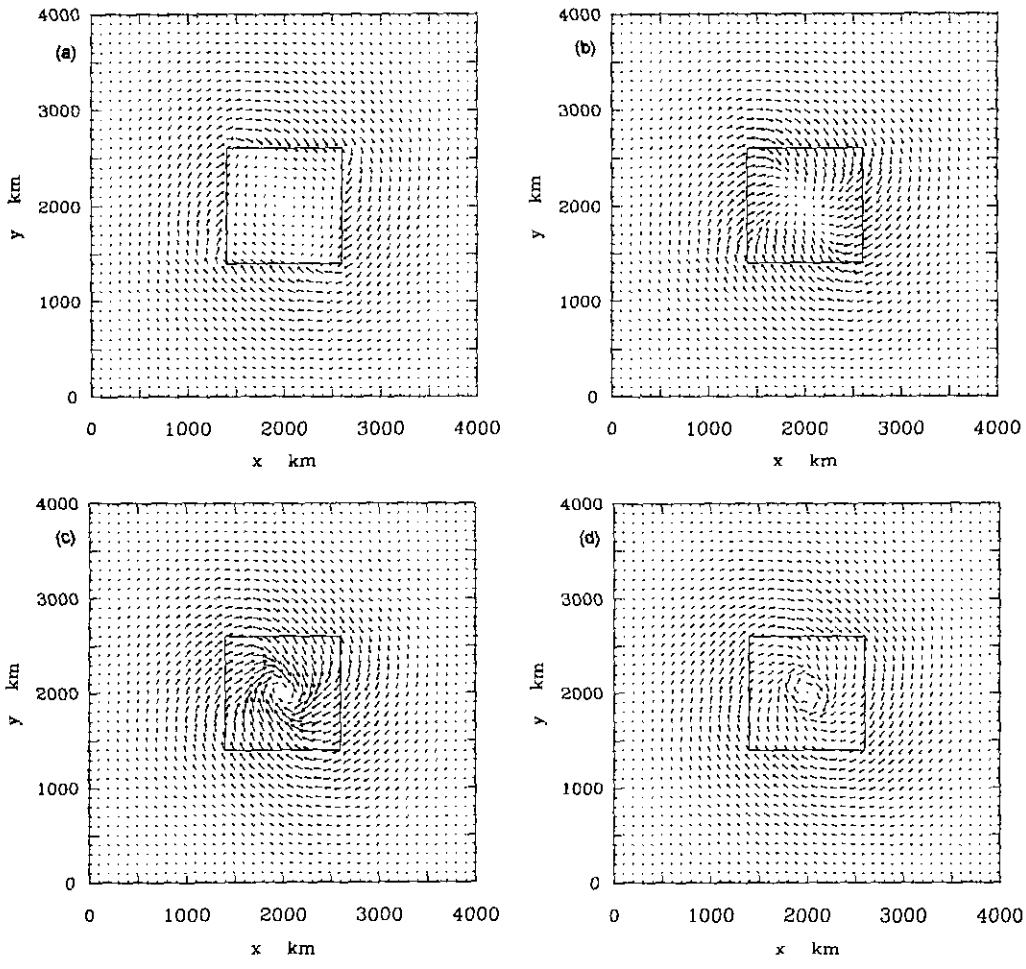

Figure 14. Wind vectors at a height of 100 m for experiment E3 at: (a) 1500 h and (b) 2100 h on day 11, and (c) 0300 h and (d) 0900 h on day 12.

former case, inertia-gravity waves are excited, while in the latter they are not. We conclude that frictional and/or nonlinear effects are sufficiently large in our calculations to render Rotunno's analysis inapplicable.

5. Discussion and conclusions

We have investigated the dynamics of a heat low in a quiescent environment using an idealized numerical model with a relatively sophisticated boundary-layer representation. The calculations help one to understand observed aspects of heat lows, including their shallow nature, the existence of a convergent cyclonic circulation at low levels and a divergent anticyclonic circulation aloft, and the late afternoon timing of the lowest minimum surface pressure. These features occur in the absence of larger-scale circulations that produce subsidence throughout much of the free troposphere and lead us to conclude, contrary to the suggestion of Blake *et al.* (1983), that the latter effect is not crucial to

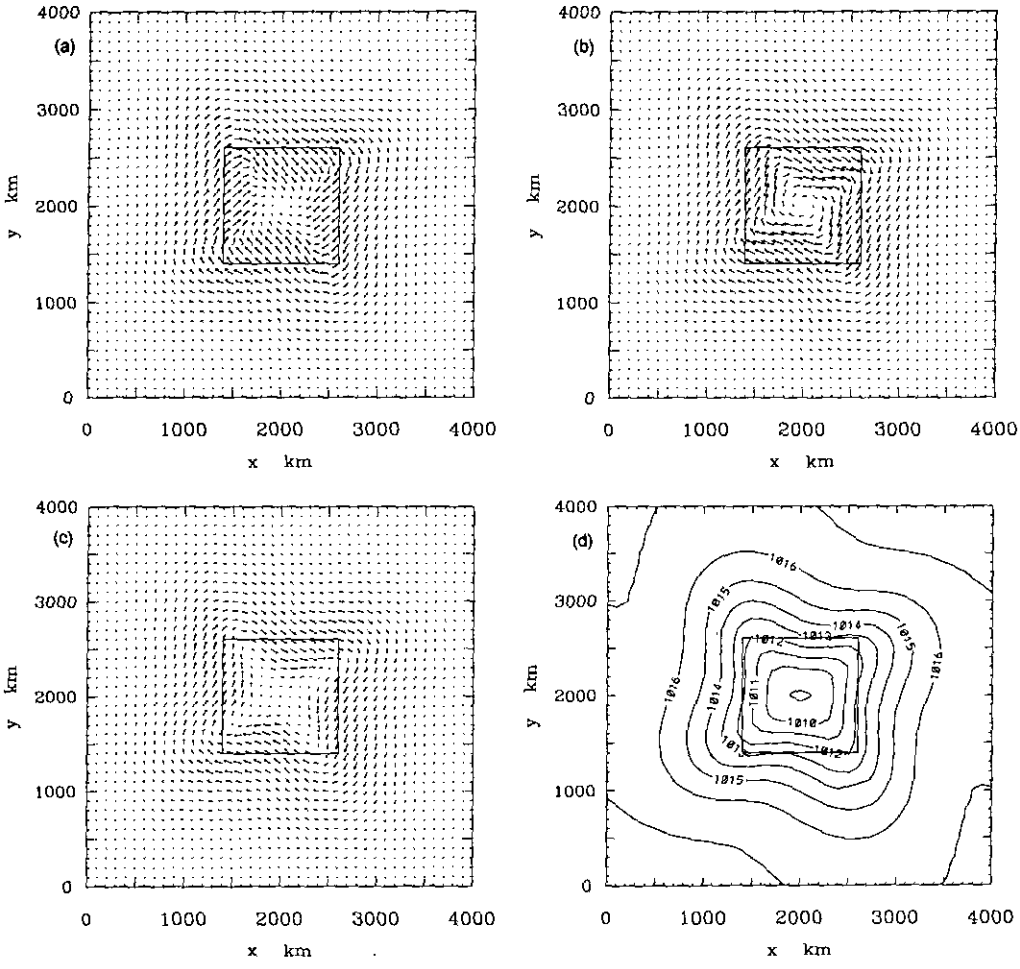

Figure 15. Wind vectors at a height of 100 m for experiment E4 at: (a) 2100 h on day 11, and (b) 0300 h and (c) 0900 h on day 12. Panel (d) shows the isobars of surface pressure (mb) for E4 at 0900 h on day 12.

understanding heat-low dynamics. The calculations point to the important contributions of the sea breeze and the nocturnal low-level jet in producing low-level convergence into the heat low during the evening and early morning hours, leading to a maximum in low-level cyclonic vorticity early in the morning. On the other hand, the relative-vorticity signature is weak during the afternoon when the convective mixing is at its peak. These results are certainly in accord with the observations of dry frontal troughs over central and northern Australia, which show a marked diurnal variation in intensity with a pronounced early morning maximum (e.g. Smith *et al.* 1995). During the day, the fronts are difficult to detect, at least at the surface where observational data are readily available. We conjecture that the main difference in behaviour between a heat trough and a frontal trough over the continent resides in the broad-scale horizontal temperature gradient across the trough and the low-level horizontal deformation of the flow, which together determine the rate of nocturnal frontogenesis within the trough. In the calculations described here, the only such temperature gradient is associated with the land–sea temperature contrast and there

is no horizontal deformation flow; the only frontogenesis is that associated with the sea breeze.

The strong low-level convergence into the heat trough or frontal trough at night may explain some observations of the generation of nocturnal bore-like disturbances over central and northern Australia; it may explain also the generation of nocturnal thunderstorms that are sometimes observed in the vicinity of the trough.

The heat trough is associated with an anticyclonic potential-vorticity perturbation in the lower troposphere on account of the greatly reduced static stability in the convective mixed layer. Moreover, because the mixed layer persists over land except near the surface, the potential vorticity shows little diurnal variation in contrast to the relative vorticity. The existence of an anticyclonic potential-vorticity anomaly is not inconsistent with a cyclonic circulation in the heat low because the surface temperature maximum in the low is equivalent to a cyclonic potential-vorticity perturbation at the surface.

In reality, the behaviour of a heat low or heat trough can be expected to be influenced by irregularities in the distribution of land, the presence of orography, the presence of an environmental flow, and transience of this flow. Notwithstanding these influences, which hopefully will be considered in a future paper, it is reasonable to presume that the processes we have described are fundamental to heat-trough behaviour, and that they operate in all arid regions of the world where deep dry convection occurs during the daytime and where there is strong surface cooling at night.

Acknowledgements

We are grateful to Lance Leslie for allowing us to use his numerical model, to Kevin Tory who provided his version of the model, and to Wolfgang Ulrich who gave much advice on the implementation of the model on the Munich computer. We are grateful also to Dan Keyser for his thoughtful critique of the original manuscript.

Appendix—Model equations

The model equations and physical parametrizations are described below. The values of various constants used in the calculations are listed in subsection (i).

(a) *Basic equations*

The horizontal-momentum equation in vector form is

$$\frac{\mathrm{D}\mathbf{u}}{\mathrm{D}t} = -RT\nabla_\sigma \ln p_s - \nabla_\sigma \phi - f\mathbf{k} \wedge \mathbf{u} + \mathbf{F}_{\mathrm{diab}} + \mathbf{F}_{\mathrm{diff}}, \tag{A.1}$$

where $\mathbf{u}$ is the horizontal wind vector; p_s is the surface pressure; T is the absolute temperature; $\phi = gz$ is the geopotential, where g is the acceleration due to gravity and z is height; f the Coriolis parameter; R is the specific gas constant; $\mathbf{F}_{\mathrm{diab}}$ and $\mathbf{F}_{\mathrm{diff}}$ represent the contributions to the frictional force from the vertical and horizontal eddy diffusion processes; and

$$\frac{\mathrm{D}}{\mathrm{D}t} = \left(\frac{\partial}{\partial t}\right)_\sigma + \mathbf{u} \cdot \nabla_\sigma + \dot{\sigma}\frac{\partial}{\partial \sigma} \tag{A.2}$$

is the total derivative. The hydrostatic equation and continuity equation are respectively:

$$\frac{\partial \phi}{\partial \sigma} = -\frac{RT}{\sigma}, \tag{A.3}$$

and

$$\frac{\mathrm{D}\ln p_s}{\mathrm{D}t} + \nabla_\sigma \cdot \mathbf{u} + \frac{\partial \dot{\sigma}}{\partial \sigma} = 0. \tag{A.4}$$

The surface pressure tendency equation (A.5) and the equation for the vertical σ-velocity (A.6) are obtained by integration of Eq. (A.4) using the boundary condition at $\sigma = 1$ and $\sigma = 0$.

$$\frac{\partial p_s}{\partial t} = -\int_0^1 \nabla \cdot (p_s \mathbf{u}) \mathrm{d}\sigma \tag{A.5}$$

$$\dot{\sigma} = -\frac{1}{p_s}\left(\sigma \frac{\partial p_s}{\partial t} + \int_0^\sigma \nabla \cdot (p_s \mathbf{u}) \mathrm{d}\sigma\right). \tag{A.6}$$

The thermodynamic equation has the form

$$\frac{\mathrm{D}T}{\mathrm{D}t} = \frac{RT}{c_p}\left(\frac{\mathrm{D}\ln p_s}{\mathrm{D}t} + \frac{\dot{\sigma}}{\sigma}\right) + (\dot{Q}_{\mathrm{diab}} + \dot{Q}_{\mathrm{diff}})\left(\frac{\sigma p}{p_o}\right)^{\frac{R}{c_p}}, \tag{A.7}$$

where c_p is the specific heat capacity at constant pressure, $p_o = 1000$ mb is a reference pressure, and $\dot{Q}_{\mathrm{diab}}$ and $\dot{Q}_{\mathrm{diff}}$ represent the contributions to the total heating from the vertical and horizontal diffusion of heat.

The vertical velocity w shown in Figs. 6–9 is computed using the approximate formula

$$w \approx -\frac{1}{g\rho}\left(p_s \dot{\sigma} - \sigma \int_0^1 \nabla \cdot (p_s \mathbf{u}) \mathrm{d}\sigma\right), \tag{A.8}$$

where ρ is the density of air.

(b) *Horizontal diffusion*

The horizontal diffusion terms in Eqs. (A.1) and (A.7) are given in terms of a fourth-order diffusion operator (Williamson 1978) by

$$\mathbf{F}_{\mathrm{diff}} = -K_{\mathrm{diff}} \nabla^4 \mathbf{u} \tag{A.9}$$

$$\dot{Q}_{\mathrm{diff}} = -K_{\mathrm{diff}} \nabla^4 \theta \tag{A.10}$$

where

$$K_{\mathrm{diff}} = (\Delta s)^2 \left[K_o + \frac{1}{2}(k\Delta s)^2 \left\{\left(\frac{\partial u}{\partial x} - \frac{\partial v}{\partial y}\right)^2 + \left(\frac{\partial v}{\partial x} + \frac{\partial u}{\partial y}\right)^2\right\}^{1/2}\right], \tag{A.11}$$

Δs is the grid spacing (the same in both the x and y directions), K_o is a constant and k is von Kármán's constant.

(c) *Diabatic processes*

The diurnal cycle is determined by the radiative heating and cooling of the surface. Heat is transferred from or to the surface by turbulent diffusion, and between the surface and the soil by thermal conduction.

The sensible-heat flux and momentum flux in the near-surface layer are calculated using similarity theory with the flux profile of Dyer (1974). Above this layer the fluxes are calculated using the Mellor–Yamada $2\frac{1}{4}$-scheme (Mellor and Yamada 1982) in the

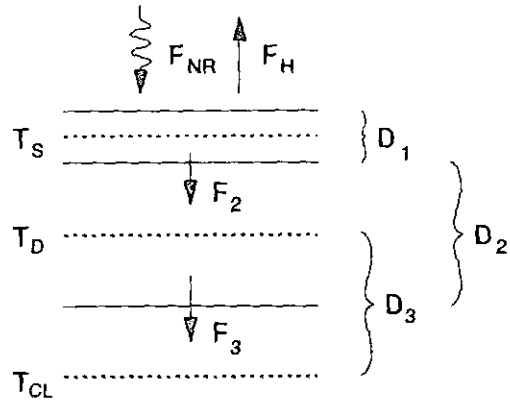

Figure A.1. Schematic diagram of the three-level soil model. The layer depths are D_1, D_2 and D_3. The temperatures. T_S and T_D are averages over the depths of the upper and middle layers, respectively, while that of the lowest soil layer, T_{CL}, is a constant climatological value. The quantities F_{NR} and F_H represent the net radiative flux and the sensible-heat flux while F_2 and F_3 represent the fluxes between the soil layers. (From Tory 1997.)

form proposed by Galperin *et al.* (1988). The surface fluxes of momentum and heat are parametrized using the scheme of Louis (1979).

The surface temperature results from a balance between the net incoming and outgoing radiation, F_{NR}, and the sensible-heat flux to the deep soil layers, F_2, and to the atmosphere, F_H (see Fig. A.1). The surface temperature tendency equation relates to a thin surface layer of soil of depth D_1 and average temperature T_s and has the form

$$\frac{\partial T_s}{\partial t} = \frac{F_{NR} - F_H - F_2}{\rho_G c_G D_1}, \tag{A.12}$$

where ρ_G is the soil density and c_G is the specific heat capacity of the soil.

(*d*) *Radiation flux*

The net radiation flux at the surface F_{NR} is the sum of the short-wave solar radiation (the first term in A.13) and the long-wave terrestrial radiation (the second term in A.13).

$$F_{NR} = (1 - A)F_o \cos\theta_o + (1 - 0.7)\sigma_b \varepsilon T_s^4, \tag{A.13}$$

where A is the surface albedo, F_o the solar constant, θ_o the zenith angle, σ_b the Stefan–Boltzmann constant, ε the emissivity, and 0.7 is the fraction of long-wave radiation that is re-radiated back from the atmosphere to the earth's surface.

(*e*) *Soil heat flux*

A simple three-layer model is used to calculate the heat flux in the soil (ECMWF 1984)—see Fig. A.1. The middle layer has a depth $D_2(= 6D_1)$ and an average temperature T_D. The heat flux F_2 is proportional to the temperature gradient and to the thermal conductivity κ.

$$F_2 = \rho_G c_G \frac{(T_S - T_D)\kappa}{\frac{1}{2}(D_1 + D_2)}. \tag{A.14}$$

The third layer has depth D_3 and the constant climatological temperature T_{CL}. The heat flux, F_3, between the middle and lower layer is analogous to (A.14):

$$F_3 = \rho_G c_G \frac{(T_D - T_{CL})\kappa}{D_3}. \tag{A.15}$$

As for the surface temperature there is a prognostic equation for T_D, namely

$$\frac{\partial T_D}{\partial t} = \frac{F_2 - F_3}{\rho_G c_G D_3}. \tag{A.16}$$

(f) Sensible-heat flux to the atmosphere

In order to solve the surface temperature equation (A.12) we need the flux of sensible heat to the atmosphere. For the first layer above the surface, between $\sigma = 1$ and $\sigma = \sigma_{30}$ (see Fig. 2(b)), this is calculated using similarity theory and a bulk transfer coefficient C_H, i.e.

$$F_H = -\rho c_p C_H |\mathbf{u}|_{\sigma_{30}} (\theta_{\sigma_{30}} - \theta_s) \tag{A.17}$$

where θ_s is the potential temperature at the surface and $|\mathbf{u}|_{\sigma_{30}}$ is the wind speed at σ_{30}, the first σ-level above the surface. Above the surface layer the heat flux is represented by

$$F_H = -\rho c_p K_H \frac{\partial \theta}{\partial z} \tag{A.18}$$

where K_H is the eddy diffusivity for heat. This is calculated in terms of eddy-correlation terms using the $2\frac{1}{4}$-closure scheme discussed by Galperin *et al.* (1988, p. 58). This scheme is a slightly simplified version of the Mellor and Yamada (1982) $2\frac{1}{2}$-closure scheme. The correlation terms depend on the turbulent eddy kinetic energy, a prognostic equation for which is carried in the model.

The contribution $\dot{Q}_{diab}$ in the thermodynamic equation (A.7) is expressed by:

$$\dot{Q}_{diab} = -\frac{1}{\rho c_p} \frac{\partial F_H}{\partial z}. \tag{A.19}$$

(g) Momentum flux to the surface

The momentum flux is calculated in the surface layer between $\sigma = 1$ and $\sigma = \sigma_{30}$, using the formula:

$$\mathbf{F}_M = -\rho C_D |\mathbf{u}|_{\sigma_{30}} \mathbf{u}_{\sigma_{30}}. \tag{A.20}$$

where C_D is the drag coefficient. Above the surface layer, $\sigma < \sigma_{30}$, F_M is given by the equation

$$\mathbf{F}_M = -\rho K_M \frac{\partial \mathbf{u}}{\partial z}. \tag{A.21}$$

where K_M is the eddy diffusivity for momentum. Then the contribution to $\mathbf{F}$ in the momentum equation is

$$\mathbf{F}_{diab} = -\frac{1}{\rho} \frac{\partial F_M}{\partial z}.$$

(h) Numerical method of solution

The equations are integrated in time in two stages using the explicit two-time-level Miller–Pearce scheme. The horizontal advection terms are represented by a third-order upwinding scheme. Details of the grid layout are given in section 2.

(i) *Parameter values*

The parameter values used in the calculations are listed in Table A.1.

TABLE A.1. PHYSICAL PARAMETERS IN THE MODEL

Parameter	Symbol	Value
Surface albedo	A	0.3
Specific heat of dry air at constant pressure	c_p	1004.67 m^2s^{-2} K^{-1}
Thickness of the first soil layer	D_1	7.2 cm
Thickness of the second soil layer	D_2	43.2 cm
Thickness of the third soil layer	D_3	43.2 cm
Coriolis parameter	f	$-4.988 \times 10^{-5}s^{-1}$
Solar constant	F_0	1365 W m^2
Gravitational acceleration	g	9.806 m s^{-2}
von Kármán's constant	k	0.4
Diffusion parameter	K_0	3×10^5 m^2s^{-1}
Reference pressure	p_0	1000 mb
Specific gas constant for dry air	R	287.04 $m^2s^{-2}K^{-1}$
Sea surface temperature	T_s	25 °C
Deep-soil temperature	T_{CL}	25 °C
Surface roughness length for momentum over land	z_{ol}	10 cm
Surface roughness length for momentum over sea	z_{os}	1 cm
Surface roughness length for heat over land	z_{hl}	$z_{ol}/10$
Surface roughness length for heat over sea	z_{hs}	$z_{os}/4.5$
Thermal emissivity	ε	0.98
Thermal conductivity	κ	$7.5 \times 10^{-7}m^2s^{-1}$
Stefan–Boltzmann constant	σ_b	5.67×10^{-8} W $m^{-2}K^{-4}$
Surface density × specific heat of the soil	$\rho_G c_G$	2.40×10^6 J $K^{-1}m^{-3}$

REFERENCES

Ackerman, S. A. and Cox, S. K. 1982 The Saudi Arabian heat low: Aerosol distribution and thermodynamic structure. *J. Geophys. Res.*, **87**, 8991–9002

Adams, M. 1986 A theoretical study of the inland trough of northeastern Australia. *Aust. Meteorol. Mag.*, **34**, 85–92

1993 A linear study of the effects of heating and orography on easterly airstreams with particular reference to northern Australia. *Aust. Meteorol. Mag.*, **42**, 69–80

Alonso, S., Portela, A. and Ramis, C. 1994 First considerations on the structure and development of the Iberian thermal low-pressure system. *Ann. Geophys.*, **12**, 457–468

Anthes, R. A. 1974 The dynamics and energetics of mature tropical cyclones. *J. Geophys. Space Phys.*, **12**, 495–522

Bitan, A. and Sa'aroni, H. 1992 The horizontal and vertical extension of the Persian Gulf pressure trough. *Int. J. Climatol.*, **12**, 733–747

Blake, D. W., Krishnamurti, T. N., Low-Nam, S. V. and Fein, J. S. 1983 Heat low over the Saudi Arabian desert during May 1979 (Summer MONEX). *Mon. Weather Rev.*, **111**, 1759–1775

Chang, J. H. 1972 Pp. 298–319 in *Atmospheric circulation systems and climate*. Oriental Publishing Co., Honolulu, Hawaii

Clarke, R. H., Dyer, A. J., Brook, R. R., Reid, D. G. and Troup, A. J. 1971 'The Wangara experiment: boundary layer data'. Tech. Paper 19. Div. Meteorol. Phys., CSIRO, Australia

Douglas, M. W. and Li, S. 1996 Diurnal variation of the lower-troposphere flow over the Arizona low desert from SWAMP-1993 observations. *Mon. Weather Rev.*, **124**, 1211–1224

Dyer, A. J. 1974 A review of flux-profile relationships. *Boundary Layer Meteorol.*, **7**, 363–372

ECMWF Research Department 1984 'Research manual 3: ECMWF forecast model parameterization'. Ed. J. F. Louis. European Centre for Medium-Range Weather Forecasts, Shinfield Park, Reading, UK

Fandry, C. B. and Leslie, L. M. 1984 A two-layer quasi-geostrophic model of summer trough formation in the Australian subtropical easterlies. *J. Atmos. Sci.*, **41**, 807–818

Gaertner, M. A., Fernández, C. and Castro, M. 1993 A two-dimensional simulation of the Iberian summer thermal low. *Mon. Weather Rev.*, **121**, 2740–2756

Galperin, B., Kantha, L. H., Hassid, S. and Rosati, A. 1988 A quasi-equilibrium turbulent energy model for geophysical flows. *J. Atmos. Sci.*, **45**, 55–62

Griffiths, J. F. and Soliman, K. H. 1972 'The northern desert'. Pp. 75–111 in *World survey of climatology, Vol. 10, Climates of Africa*. Ed. J. F. Griffiths. Elsevier

Hoskins, B. J., McIntyre, M. E. and Robertson, A. W. 1985 On the use and significance of isentropic potential vorticity maps. *Q. J. R. Meteorol. Soc.*, **111**, 877–946

Joshi, P. C. and Desai, P. S. 1985 The satellite-determined thermal structure of heat lows during Indian south-west monsoon season. *Adv. Space Res.*, **5**, 57–60

Junning, L., Zhengan, Q. and Fumin, S. 1986 'An investigation of the summer lows over the Qinghai–Xizang plateau'. Pp. 369–386 in *Proceedings of the international symposium on the Qinghai–Xizang plateau and mountain meteorology*. 20–24 March 1984, Beijing, China. American Meteorological Society 1986, Boston, Mass., USA

Kepert, J. D. and Smith, R. K. 1982 A simple model of the Australian west coast trough, *Mon. Weather Rev.*, **120**, 2042–2055

Leighton, R. and Deslandes, R. 1991 'Monthly anticyclonicity and cyclonicity in the Australian region: 23-year averages'. Tech. Rep. No. 64, Bureau of Meteorology. (Available from the Bureau of Meteorology, PO Box 1289K, Melbourne, Australia, 3001.)

Leslie, L. M. 1980 Numerical modelling of the summer heat low over Australia. *J. Appl. Meteorol.*, **19**, 381–387

Leslie, L. M. and Skinner, T. C. 1994 Real-time forecasting of the western Australian summertime trough: Evaluation of a new regional model. *Weather and Forecasting*, **9**, 371–383

Leslie, L. M., Mills, G. A., Logan, L. W., Gauntlett, D. J., Kelly, A. G., Manton, M. J., McGregor, J. L. and Sardie, J. M. 1985 A high resolution primitive equations NWP model for operations and research, *Aust. Meteorol. Mag.*, **33**, 11–35

Louis, J. F. 1979 A parametric model of vertical eddy fluxes in the atmosphere, *Boundary-Layer Meteorol.*, **17**, 187–202

Mellor, G. and Yamada, T. 1982 Development of a turbulent closure model for geophysical fluid problems. *Rev. Geophys. Space Phys.*, **20**, 851–875

Moriarty, W. W. 1955 'Large-scale effects of heating over Australia. I. The synoptic behaviour of the summer low'. Tech. Paper No. 7. Div. Meteorol. Phys., CSIRO, Australia

Neumann, J. and Mahrer, Y. 1974 A theoretical study of the sea and land breezes over circular islands. *J. Atmos. Sci.*, **31**, 2027–2039

Portela, A. and Castro, M. 1996 Summer thermal lows in the Iberian peninsula: A three-dimensional simulation. *Q. J. R. Meteorol. Soc.*, **122**, 1–22

Pedgley, D. E. 1972 Desert depressions over north-east Africa. *Meteorol. Mag.*, **101**, 228–244

Ramage, C. S. 1971 Pp. 25–100 in *Monsoon meteorology*. Academic Press, New York, USA

Rotunno, R. 1983 On the linear theory of the land and sea breeze. *J. Atmos. Sci.*, **40**, 1999–2009

Rowson, D. R. and Colucci, S. J. 1992 Synoptic climatology of thermal low-pressure systems over south-western North America. *Int. J. Climatol.*, **12**, 529–545

Sellers, W. D. and Hill, R. H. 1974 *Arizona climate*. University of Arizona Press, Tucson, USA

Shapiro, L. J. and Ooyama, K. V. 1990 Barotropic vortex evolution on a beta plane. *J. Atmos. Sci.*, **47**, 170–187

Smith, E. A. 1986a The structure of the Arabian heat low. Part I: Surface energy budget. *Mon. Weather Rev.*, **114**, 1067–1083

1986b The structure of the Arabian heat low. Part II: Bulk tropospheric heat budget and implications. *Mon. Weather Rev.*, **114**, 1084–1102

Smith, R. K. and Leslie, L. M. 1975 Thermally driven vortices: a numerical study with application to dust-devil dynamics. *Q. J. R. Meteorol. Soc.*, **102**, 791–804

Smith, R. K., Ulrich, W. and Dietachmayer, G. 1990 A numerical study of tropical cyclone motion using a barotropic model. I: The role of vortex asymmetries. *Q. J. R. Meteorol. Soc.*, **116**, 337–362

Smith, R. K., Reeder, M. J., Tapper, N. J. and Christie, D. R. 1995 Central Australian cold fronts. *Mon. Weather Rev.*, **123**, 16–38

Stull, R. B. 1988 *An introduction to boundary-layer meteorology*. Atmospheric Sciences Library. Kluwer, Dordrecht, the Netherlands

Tory, K. 1997 'The effect of the continental planetary boundary layer on the evolution of fronts'. Ph.D. dissertation, Monash University

Uriarte, A. 1980 Rainfall on the northern coast of the Iberian peninsula. *J. Meteorol.*, **5**, 138–144

Williamson, D. L. 1978 The relative importance of resolution, accuracy and diffusion in short-range forecasts with the NCAR global circulation model. *Mon. Weather Rev.*, **106**, 69–88